

# Charge distribution as a molecular modulator of the nanostructuration in intrinsically disordered protein polymers

*Sergio Acosta, Leander Poocha, Luis Quintanilla-Sierra, and J. Carlos Rodríguez-Cabello\**

Bioforge lab, CIBER-BBN, University of Valladolid, Paseo Belén 19, 47011, Valladolid, Spain

[\\*roca@bioforge.uva.es](mailto:*roca@bioforge.uva.es)

**KEYWORDS.** Intrinsically disordered protein polymers, charge, self-assembly, phase transition, elastin

**ABSTRACT.** Intrinsically disordered protein polymers (IDPPs) have attracted a lot of attention in the development of bioengineered devices and use as molecular biology study models due to their biomechanical properties and stimuli-responsiveness. The present work aims to understand the effect of charge distribution on self-assembly of IDPPs. To that end, a library of recombinant IDPPs based on an amphiphilic diblock design with different charge distributions were bioproduced and their supramolecular assembly characterized on the nano-, meso- and microscale. Although phase transition was driven by the collapse of hydrophobic moieties, hydrophilic block composition strongly affected hierarchical assembly and, therefore, enabled the production of new molecular

architectures, thus leading to new dynamics that govern the liquid-gel transition. These results highlight the importance of electrostatic repulsion for the hierarchical assembly of IDPPs and provide insights into the fabrication of supramolecular protein materials.

## 1. Introduction

Supramolecular materials resulting from the hierarchical assembly of peptides and proteins have gained increasing interest in recent years due to their application in materials science, biotechnology and biomedicine.<sup>1,2</sup> Intrinsically disordered protein polymers (IDPPs) that exhibit stimuli-responsive behavior are of particular relevance.<sup>3,4</sup> IDPPs are polypeptides composed of repetitions of low complexity sequences found in intrinsically disordered proteins (IDPs), which confers them the ability to undergo phase transitions in solution (i.e. lower critical solution temperature (LCST) or upper critical solution temperature (UCST) behavior).<sup>4</sup> This property of stimuli-responsiveness and the fact that these IDPPs are produced by recombinant synthesis enable the controlled biofabrication of advanced self-assembling nanosystems with bespoke properties. Additionally, they constitute a powerful tool for studying the structural properties that are responsible for phase transition of complex IDPs and the subsequent formation of protein-rich biomolecular condensates.<sup>5-8</sup>

One of the most important families of IDPPs that has received increased attention in biomedical studies and applications are elastin-like recombinamers (ELRs).<sup>4</sup> These protein-engineered polymers are structurally based on the conserved motifs of tropoelastin, generally based on the pentapeptide with a sequence  $X_1$ -Pro-Gly- $X_2$ -Gly (where  $X_1$  can be Val or Ile and  $X_2$  can be any amino acid except L-Pro).<sup>9,10</sup> ELRs exhibit excellent biocompatibility and a LCST phase behavior, which can be tuned at a molecular level during the design of the polymer chain.<sup>11</sup> This recombinant synthesis enables the rational design of hierarchically assembled protein nanosystems, including micelles, vesicles and physical hydrogels, with potential application in biotechnology and materials engineering.<sup>12,13</sup>

Electrostatic interactions between ionic amino acids are one of the parameters that mediate self-assembling of IDPs and IDPPs.<sup>14-16</sup> Indeed, the presence of ionic amino acids contribute to phase transition and folding of ELRs and ELR-based bioconjugates,<sup>17,18</sup> enabling the production of innovative supramolecular nanomaterials.<sup>19</sup> Whereas non-ionic elastin-like diblock co-recombinamers (ELdcRs) are known to self-assemble into spherical micelles in solution,<sup>20-23</sup> incorporation of ionic amino acid residues into the hydrophilic block has been shown to lead to not only to the formation spherical micelles but also to more complex supramolecular architectures, such as cylindrical assemblies,<sup>24</sup> pearl-necklace-like structures,<sup>25</sup> fibers and lamellae.<sup>26-28</sup> However, the effect of charge distribution on the self-assembly of IDPPs has not yet been considered.

Herein, this study aims to evaluate the influence of charge distribution and density on the phase transition and subsequent supramolecular assembly of model IDPPs (ELRs) in order to shed light on the design rules of IDPs-based engineered materials. The length and charge density of amphiphilic diblocks designs were varied to *de novo* biosynthesize a library of ELdcRs. Circular dichroism (CD) spectroscopy, dynamic light scattering (DLS), turbidity measurements, transmission and scanning electron microscopy (TEM and SEM) and micro- and macrorheological characterization were performed in order to obtain a comprehensive overview of thermal behavior and hierarchical self-assembly of the ionic ELdcRs on the nano-, meso- and microscale. We show the self-assembly of ionic ELdcRs into hierarchical architectures, from the solute state to physical hydrogels, via the formation of supramicellar assemblies. On the basis of the results, electrostatic repulsion is seen to be a critical parameter for nanostructure complexity of IDPPs, and charge distribution can be used to tune the hierarchical

assembly into supramicellar assemblies and physical hydrogels and enable the modulation of their mechanical properties.

## **2. Experimental section**

### **2.1. Synthesis and characterization of ELdcRs library**

All ELdcRs were recombinantly produced as described elsewhere.<sup>29</sup> Briefly, the ELdcR-encoding genes were constructed into a pDrive vector in *Escherichia coli* XL-1 blue (Agilent, USA) then cloned into a pET-25b (+) vector for expression in *E coli* BLR (DE3) strain. After bacterial fermentation in a 15-L bioreactor (Applikon biotechnology, USA), the ELdcRs were purified by inverse transition cycling (ITC) using 1.5 M NaCl for precipitation. Pure products were dialyzed against deionized and ultrapure water (12,000 MwCO, Medicell Membranes Ltd, UK), neutralized with NaOH (pH $\approx$ 7.0), filtered (0.22  $\mu$ m Nalgene<sup>TM</sup>, ThermoFisher Scientific, USA), lyophilized and stored at -20 °C until further use. A final yield of 425-640 mg L<sup>-1</sup> of cells was obtained, depending the diblock construct.

The monodispersity and purity of the ELdcRs were evaluated by sodium dodecyl sulfate–polyacrylamide gel electrophoresis (SDS-PAGE), matrix-assisted laser desorption/ionization time-of-flight (MALDI-TOF) mass spectrometry and by high performance liquid chromatography (HPLC). MALDI-TOF and HPLC were carried out in the Laboratorio de Técnicas Instrumentales (LTI) at the University of Valladolid.

The theoretical hydrophobicity of the ELdcRs was calculated using the ProtScale algorithm and the Kyte-Doolittle scale.<sup>30,31</sup> The algorithm predicts the hydrophilic and hydrophobic tendencies of a polypeptide chain by the progressive evaluation (from the N-terminus to the C-terminus) of the average hydropathy following the Kyte-Doolittle

scale, where the larger the number is, the more hydrophobic the amino acid. The most hydrophilic amino acids are arginine (-4.5) and lysine (-3.9), whereas the most hydrophobic ones are isoleucine (4.5) and valine (4.2).

## **2.2. Transition temperature analysis by turbidimetry**

Transition temperatures ( $T_i$ ) were determined by measuring the optical density at 350 nm ( $OD^{350}$ ) of ELdcRs in ultrapure water at different concentrations (25, 50, 125, 250 and 500  $\mu\text{M}$ ) on a Cary 100 UV-Vis multicell spectrophotometer (Agilent). Data were collected between 5 and 50  $^{\circ}\text{C}$  at 1  $^{\circ}\text{C min}^{-1}$  scan rate in triplicates. The transition temperature was determined as the temperature value corresponding to the maximum of the first derivative of the turbidity as a function of the temperature.

## **2.3. Nanostructure size analysis by dynamic light scattering**

The nanostructure sizes were calculated in ultrapure water using a Zetasizer Nano (Malvern Instruments, UK), with a  $173^{\circ}$  scattering angle and equipped with a HeNe laser (633 nm) with an output power of 10 mW. Nanostructures formation was monitored by measuring the derived count rate (DCR), which is the mean scattered intensity normalized by the attenuation factor, and the hydrodynamic diameter of the resulting structures every 2.5  $^{\circ}\text{C}$  from 10 to 50  $^{\circ}\text{C}$ . Samples were stabilized for 2 min at each temperature and measured in triplicate, with 11 runs per measurement. Size distribution of the ELdcRs was also analyzed in a range of concentrations (25–250  $\mu\text{M}$ ) at 37  $^{\circ}\text{C}$  to evaluate the effect of the concentration of the polymer chains on self-assembly.

## **2.4. Circular dichroism spectroscopy**

Circular dichroism (CD) spectra were recorded using a Jasco J-810 spectropolarimeter (Jasco, USA) equipped with a temperature controller (Research Technical Services, University of Alicante, Spain). Samples were dissolved at 0.2 mg mL<sup>-1</sup> and measured in 0.1 cm quartz cells in the range 190-250 nm. The temperature was stabilized at 37 °C for 10 min prior to measurement. Secondary structure percentages were determined using the BeStSel (Beta Structure Selection) web server<sup>32,33</sup> in the 200-250 nm range (when the dynode voltage was below 500 volts). Data were smoothed using a 15pt Savitzky-Golay filter.

### **2.5. Negative-stain transmission electron microscopy**

Negative-stain transmission electron microscopy (TEM) samples were prepared on 300-mesh carbon coated copper grids (C300Cu) with negative staining. To that end, grids were rendered hydrophilic by plasma treatment using a PDC-002 plasma cleaner (Harrick Plasma, USA). Low power setting (7.2 W applied to the RF coil) for 20 s. Then, 15 µL of the pre-incubated ELdcR solutions (1 h at 37 °C at a concentration of 25 µM), ultrapure water and uranyl acetate (1% w/v) were dropped on Parafilm<sup>®</sup> strip over a pre-heated (37 °C) glass surface. Plasma treated grids were sequentially placed on the ELdcR drop for 90 s, on ultrapure water for 60 s, and finally, on the negative staining solution for another 60 s. Blotting filter paper was used to remove excess solution after every step by touching the edge of the grid.

Images were obtained using a Tecnai Thermoionic T20 microscope operating at 200 kV (SAI, University of Zaragoza, Spain).

### **2.6. Cryogenic transmission electron microscopy**

Lyophilized ELdcRs (E-I, S-I, E<sub>1/2</sub>-I, oE-I and oE<sub>1/2</sub>-I) were dissolved to 250 and 500  $\mu\text{M}$  in pre-chilled ultrapure water and kept at 4 °C overnight, then the samples were incubated at 37 °C for 1 hour. Four microliters of sample were deposited in a freshly glow-discharged Cu 200 mesh grid (R 2/2 Holey Carbon Films; N1-C16nCu20-01; Quantifoil®, Germany) that was inside the chamber of a Vitrobot Mark III (FEI Company, USA), at 8 °C temperature and relative humidity close to saturation (90% rH). After 30 seconds of incubation, excess liquid was removed by blotting (for 3 seconds at 2 mm blot offset). After the blotting step, the grid was plunged into the liquid ethane bath, previously cooled with liquid nitrogen at approximately -180 °C. Once the specimen is frozen, the vitrified grids were removed from the plunger and stored under liquid nitrogen.

Vitrified grids were cryo-transferred (-174 °C) in a 626 DH cryo transfer holder (Gatan Inc., USA) and analyzed on a JEM-2200FS/CR transmission electron microscope (JEOL Europe, Croissy-sur-Seine, France). No-tilted zero-loss two-dimensional (2D) images were recorded under low-dose conditions, with a total dose on the order of 20-30 electrons  $\text{\AA}^{-2}$  per exposure, at defocus values ranging from 2.5 to 5.0  $\mu\text{m}$ . Digital images were recorded on a 4K  $\times$  4K (15  $\mu\text{m}$  pixels) Ultrascan4000™ charge-coupled device (CCD) camera (Gatan Inc., USA) using DigitalMicrograph™ (Gatan Inc., USA) software, at a nominal magnification of 20,000 and 30,000 $\times$  resulting in a final sampling of 5.69  $\text{\AA}$  pixel<sup>-1</sup> and 3.54  $\text{\AA}$  pixel<sup>-1</sup> respectively.

## **2.7. Passive microrheology**

Viscoelastic properties of semidilute solutions of the ELdcRs were analyzed by DLS-based passive microrheology using a Zetasizer Nano (Malvern Instruments, UK). To that end, carboxyl-functionalized melamine resin particles (MF-COOH-AR586, microParticles GmbH, Germany) with mean diameter of 1.02 $\pm$ 0.04  $\mu\text{m}$  were used as tracer particles. A volume of 15  $\mu\text{L}$  of tracer particles was mixed with 1 mL of polymer solutions at different concentrations (25, 50, 125, 250, 375 and 500  $\mu\text{M}$  in ultrapure water) at 4 °C. Tracer particles concentration was optimized in order to ensure that the

scattered signal was dominated by the tracer scattering and the intensity particle size distribution shows a monomodal distribution with a narrow peak corresponding with the size of the tracer. After tracer particles dispersion, samples were incubated at 37 °C for 30 min and the motion of the tracer particles was measured by DLS.

## **2.8. Physical hydrogel formation and characterization**

Protein polymers were dissolved in ultrapure water at a concentration of 2.5 mM at 4 °C, then incubated at 37 °C for 15 min to qualitatively test the ability to form physical hydrogels.

### *2.8.1. Scanning electron microscopy*

In order to visualize the morphology of those samples that formed hydrogels, samples were analyzed by scanning electron microscopy (SEM). To that end, lyophilized ELdcRs were dissolved in 500 µL of ultrapure water at a concentration of 2.5 mM and incubated in a rotatory agitator at 5 °C overnight. The physical hydrogels were then formed in microcentrifuge tubes by the incubation of the tubes at 37 °C for 1 h. The hydrogels were then immersed in liquid N<sub>2</sub> for 1 min, cryo-fractured and the resulting fragments of hydrogel were lyophilized. Samples were coated with a 20 nm layer of Pd using a Leica EM ACE200 vacuum coater and SEM micrographs obtained using a FEI Quanta 200 FEG (FEI Company, USA) microscope in low vacuum mode (SAI, University of Zaragoza, Spain).

### *2.8.2. Rheological analysis*

The mechanical properties of the physical hydrogels formed both at 2.5 mM and 11.7% (w/v) were tested by performing oscillatory shear and flow measurements in an AR2000 rheometer (TA Instruments) using a parallel plate with a diameter of 40 mm.

Measurements were performed with a sample volume of 1300  $\mu\text{L}$  (gap = 1100  $\mu\text{m}$ ) at 37  $^{\circ}\text{C}$ , controlling the temperature with a Peltier plate. After sample deposition at 4  $^{\circ}\text{C}$ , gel formation was accomplished *in situ*. Data were recorded using TRIOS software (v4.1.1.33073). All measurements were performed at least in triplicate.

Flow measurements were employed to measure the viscosity. Samples were conditioned with a pre-shear of 500  $\text{s}^{-1}$  for 1 min, then the viscosity was measured in a flow ramp from 500 to 0.1  $\text{s}^{-1}$  using a continuous ramp in a logarithmic descending series of discrete steps. Overall measurement took 10 min, acquiring 10 points for each order of magnitude.

For the oscillatory shear measurements, a strain sweep was performed from 0.01% to 15% at a frequency of 1 Hz to test the linear viscoelastic region (LVR). Frequency sweeps were carried out sequentially from 0.1 to 50 Hz, with a constant strain of 0.3% (corresponding to the LVR region). The storage ( $G'$ ) and loss moduli ( $G''$ ) were obtained from the rheological measurements. The loss factor ( $\tan \delta = G''/G'$ , where  $\delta$  is the phase angle between the output response to the input stimulus) and the complex modulus magnitude ( $|G^*|^2 = (G')^2 + (G'')^2$ ) were then calculated using the values obtained.

### **3. Results and discussion**

#### **3.1. Molecular design and bioproduction**

In order to study the influence of charge on self-assembly, an ELdcR library was designed based on the sequence of a diblock ELR developed previously in our group.<sup>34</sup> The original diblock design (A-B), referred to as E-I, was based on an anionic hydrophilic block E [(VPGXG)<sub>50</sub>; X=V/E in a 4:1 ratio] and a hydrophobic block I

[(XPGVG)<sub>60</sub>, X=I] (Table 1), with an LCST above and below physiological temperature, respectively. This molecular design enables the formation of self-assembled micelles or physical hydrogels depending on the concentration under physiological conditions.<sup>25</sup> In order to study the influence of charge density and size on the corona during self-assembly, the length and composition of the hydrophilic block was varied and; the hydrophobic block was the same for all constructs. Thus, four new ELdcRs were recombinantly produced as heterologous proteins in *E. coli*: i) an non-ionic diblock with the same amino acid length for the E-I but based on uncharged L-serine as polar amino acid (S-I), ii) a diblock in which the length of the charged ionic hydrophilic block E was decreased by half (E<sub>1/2</sub>-I), iii) a diblock in which only the glutamic acid pentapeptides of the original hydrophilic E-block were maintained (oE-I), and iv) a related system in which these pentapeptides were decreased by half (oE<sub>1/2</sub>-I). Condensation of the charged pentapeptides in the oE-blocks may have an impact on the hydrophathy of the block. A schematic representation of the ELdcR library designs, hydrophathy plots and complete amino acid sequences and size ratios of the ELdcRs can be found in Figure 1 and Table 1, respectively.

Purification by ITC enabled us to obtain highly pure and monodisperse products with extreme control of the sequence,<sup>35</sup> as confirmed by SDS-PAGE (Figure 1c), MALDI-TOF (Figure S1, S2 and Table S1) and HPLC (Table S2).

**Table 1.** Molecular weights (MW), hydrophilic weight fraction ( $f$ ), hydrophilic-hydrophobic block length ratio and complete sequence of the ELdcRs.

	MW (kDa)	Hydrophilic weight fraction ( $f$ )	Hydrophilic- hydrophobic ratio	Sequence
<b>E-I</b>	46.9	46%	1:1.2	MESLLP-[(VPGVG) <sub>2</sub> -VPGEG-(VPGVG) <sub>2</sub> ] <sub>10</sub> -VG-(IPGVG) <sub>59</sub> -IPGV
<b>S-I</b>	46.0	47%	1:1.2	MESLLP-(VPGSG) <sub>50</sub> - VG-(IPGVG) <sub>59</sub> -IPGV
<b>E<sub>1/2</sub>-I</b>	36.6	30%	1:2.4	MESLLP-[(VPGVG) <sub>2</sub> -VPGEG-(VPGVG) <sub>2</sub> ] <sub>5</sub> - VG-(IPGVG) <sub>59</sub> -IPGV
<b>oE-I</b>	30.6	17%	1:6	MESLLP-(VPGEG) <sub>10</sub> - VG-(IPGVG) <sub>59</sub> -IPGV
<b>oE<sub>1/2</sub>-I</b>	28.4	10%	1:12	MESLLP-(VPGEG) <sub>5</sub> - VG-(IPGVG) <sub>59</sub> -IPGV

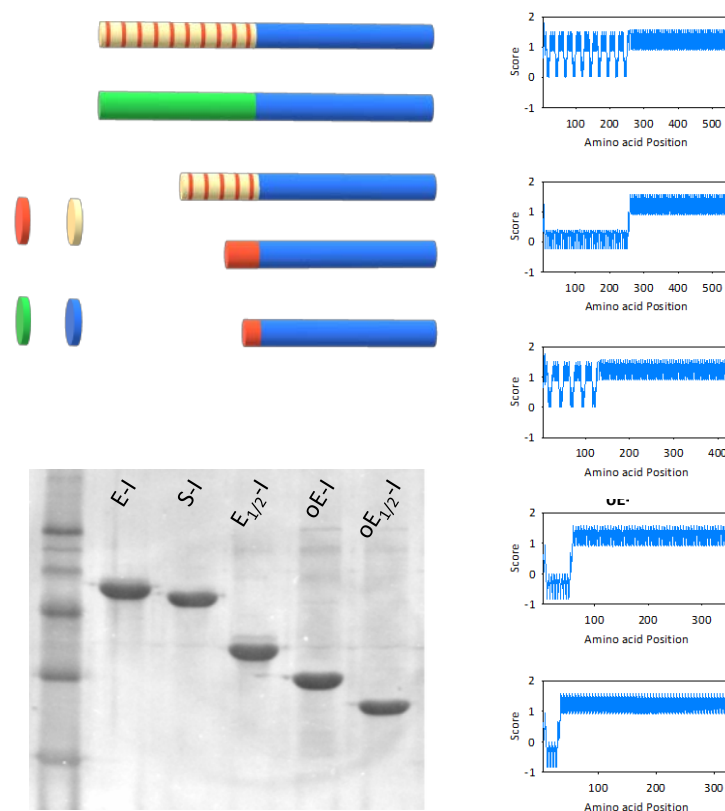


**Figure 1.** (a) Schematic representation of the ELdcR sequences (b) and their hydropathy plot calculated using the Kyte-Doolittle scale. (c) CuCl<sub>2</sub>-stained SDS-PAGE gel of the purified ELdcRs. The first lane from left to right is the Pierce™ Unstained Protein MW Marker (ThermoFisher). Lanes 2 to 6 are the different ELdcRs.

### 3.2. Thermally driven phase transition

The repetitive consensus motif (VPGXG) of ELRs encodes for thermoresponsive behavior in aqueous solutions,<sup>36</sup> which is characterized by a LCST phase transition. Since amphiphilic diblock molecular designs lead the coacervation into micellar nanostructures,<sup>21,35</sup> thermally-driven self-assembly of the ELdcRs was studied in ultrapure water in order to assess the influence of charge density and the highly asymmetric designs on phase transition in aqueous solutions. During the monitoring of the formation of nanostructures by DLS, it was observed that all the diblock co-recombinamers underwent a LCST phase transition. (Figure 2a and 2b). Below  $T_t$ , the low scattering intensity suggested complete hydration and solubility of the ELdcR molecules. When the temperature was increased above  $T_t$  of the hydrophobic block (I), the collapse of the I-block triggered the formation of micellar assemblies composed by hydrophobic cores surrounded by the hydrophilic blocks, consistent with studies by others.<sup>20,24,35</sup> As a consequence, scattering intensity (derived count rate, DCR) increased as well as the hydrodynamic diameter of the samples. It must be noted that ionic diblock designs self-assembled into larger micellar assemblies than the non-ionic diblock copolymer (S-I). While the corona length of micellar systems based on ELdcRs depends on the MW of the hydrophilic blocks,<sup>35</sup> the ionic pentapeptide monomers are also likely to have contributed to corona length of ELR nanoparticles. Electrostatic repulsion between charged residues could have potential enlarged the hydrodynamic size of the corona, thus increasing the hydrodynamic diameter ( $D_h$ ) of the micelles observed, similarly to that occurs in synthetic polyelectrolyte diblock copolymers.<sup>37</sup>

The effect of concentration of the protein polymers on the LCST phase transition and on the  $T_t$  was studied in detail by turbidimetry (Figure 2c). The chain length, concentration and the presence of ionic guest residues are crucial parameters that strongly modulate

the LCST behavior of non-ionic ELRs.<sup>17,38</sup> As expected, the effect of ionic hydrophilic blocks on  $T_t$  dominated over the molecular weight of the ELdcR. The comparison between  $T_t$  of the ionic diblock E-I (MW=46.9 kDa,  $f = 46\%$ , ionic hydrophilic block) and  $T_t$  of the non-ionic diblock S-I (MW=46.0 kDa,  $f = 47\%$ , non-ionic hydrophilic block) suggested that charged residues in diblock co-recombinamers contributed in improving the solubility of the hydrophobic I-block, thereby increasing the values of  $T_t$ . Moreover, charge distribution seemed to strongly affect the  $T_t$ . Despite the highly asymmetric designs of the oE-I and oE<sub>1/2</sub>-I co-recombinamers with a short hydrophilic block ( $f = 17\%$  and  $f = 10\%$ , respectively), increasing the charge density in the hydrophilic blocks resulted on an increase of the  $T_t$  in comparison with the ionic ELdcR analogs with larger hydrophilic blocks (E-I and E<sub>1/2</sub>-I). According to the Kyte-Doolittle plots, an increment on the density of ionic pentapeptides in the hydrophilic block correlates with an enhancement in the hydrophilicity of the hydrophilic block (Figure 2c). Besides that, charged guest residues favor the hydration of elastin-like polypeptides through enhanced hydration layer.<sup>39</sup> This, together with the fact that increased charge density and associated increased electrostatic repulsion between charged residues may result in a synergistic effect that improved the solubility of the ELdcR chain, thereby increasing the  $T_t$ .

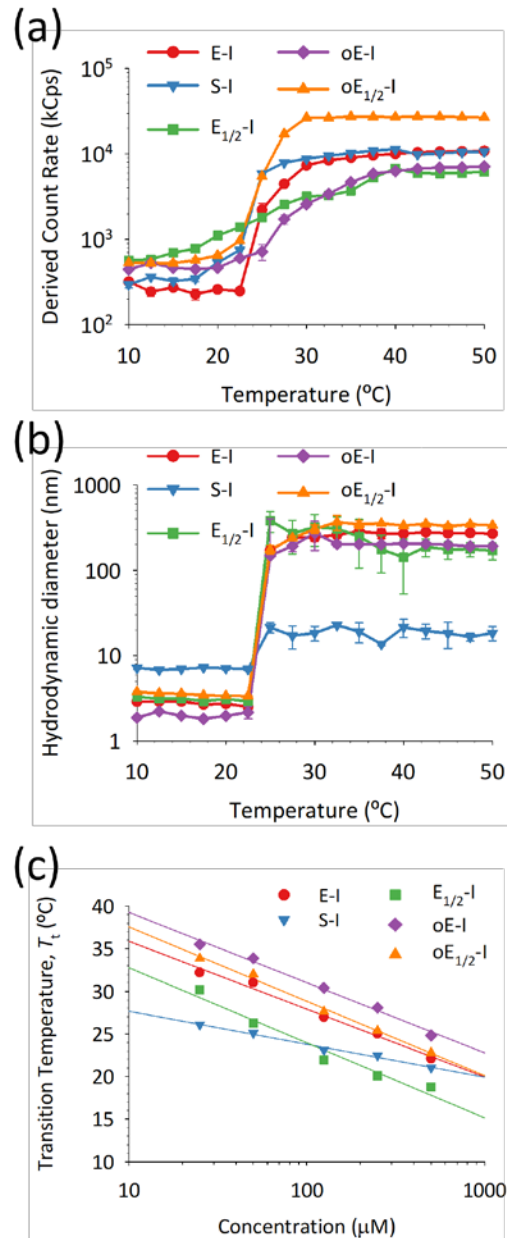


**Figure 2.** Thermally-driven self-assembly of the ELdcRs. (a) Scattering intensity (derived count rate) as a function of the temperature revealed that all the ELdcRs (25  $\mu\text{M}$ ) showed a LCST behavior with a transition temperature ( $T_t$ ) below 37  $^\circ\text{C}$ . (b) Hydrodynamic diameter of the structures as a function of the temperature obtained by DLS. Ionic ELdcRs, including highly asymmetric designs, at 25  $\mu\text{M}$  in ultrapure water led to the formation of larger micellar assemblies than non-ionic ELdcRs. (c) Transition temperatures ( $T_t$ ) of the ELdcRs as a function of the concentration measured by turbidimetry.

Thermal phase transition of the ELRs is associated with an increase in secondary structures.<sup>35</sup> CD analysis below and above  $T_t$  (Figures S3a and S3b) confirmed that LCST phase transition correlated with the formation of secondary  $\beta$ -structures (i.e.  $\beta$  turns and distorted  $\beta$ -sheet conformations), but maintaining structural disorder due to

the intrinsically disordered nature of the ELRs (“*Others*” in Figure S3). Moreover, since all the ELdcRs share the same hydrophobic block, differences in the composition of the hydrophilic blocks barely affected the content on secondary structures of the different ELdcRs (Figure 3c and 3d), as previously reported.<sup>35</sup> Below  $T_t$  (5 °C), the CD spectra showed a minimum around 197 nm, characteristic of IDPs, and a positive shoulder near 210 nm. In contrast, coacervation of the hydrophobic block induced an increase of secondary structures and as a consequence, the characteristic negative peak for elastin-like polypeptides appeared around 210 nm.<sup>36,40</sup> CD spectra above  $T_t$  also showed a still high content on random coils (peak around 197 nm), due to the intrinsically disordered nature of ELRs and the contribution of the unfolded hydrophilic blocks.

The amplitude of the signal is less pronounced for the samples oE-I and oE<sub>1/2</sub>-I, indicating a less extent of transitioning pentapeptides. For a better understanding of the underlying mechanism, the data was deconvoluted using the BeStSel algorithm (Figure S3c and S3d).<sup>32,33</sup> Accordingly to the less pronounced signals of the asymmetric ELdcRs, a decrease in ordered structures (higher amount of undefined structures) was found for highly asymmetric ionic ELdcRs. Although this did not seem to affect their self-assembly, it appears that a high charge density in the reduced and condensed hydrophilic region may favor the disordered nature of the polypeptides, mainly by reducing the anti-parallel proportion.

### **3.3. Self-assembly into nanoparticles and supramicellar structures**

Self-assembly of ELdcRs was studied at increasing polymer concentrations (25 to 500  $\mu\text{M}$  in ultrapure water) so as to discern the role of the composition of the hydrophilic block in the nanostructuration in solution. Since all the ELdcR designs share the same thermoresponsive hydrophobic block, supramolecular assembly was studied as a

function of the molar concentration in order to get insights into the influence of charge distribution and hydrophilic fraction on the nanostructuration.

TEM micrographs of ELdcR solutions at 25  $\mu\text{M}$  confirmed that all the diblocks self-assembled into spherical micelles at low concentrations (Figure 3). Decreasing the length of the ionic block led to morphological changes of the micellar assembly of synthetic diblock copolymers, characterized by a transition from spherical micelles to cylindrical (worm-like) and planar (i.e. vesicles and lamellar aggregates) structures, in agreement with findings by others in literature.<sup>37,41,42</sup> However, ionic diblock protein polymers showed a different behavior. Surprisingly, the highly asymmetric amphiphilic diblocks (oE-I and oE<sub>1/2</sub>-I) also allowed self-assembly into spherical micelles at low concentrations (Figure 4d and 4e) despite the fact that the length ratio between both blocks (Table 1) was outside the limits previously predetermined in the literature for micellar formation of non-ionic amphiphilic ELdcRs ( $1:2 \leq \text{length ratio} \leq 2:1$  and hydrophilic:hydrophobic ratio  $\geq 0.3$ ).<sup>20,23</sup> It can thus be suggested that an increment in charge density facilitates the assembly of hydrophobic blocks into spherical micelles via improved hydration of the coronal blocks. Consistent with turbidimetry results, charged residues would induce an enhanced hydration of the protein backbone and electrostatic repulsive forces would result in stretching of the coronal blocks.<sup>42</sup>

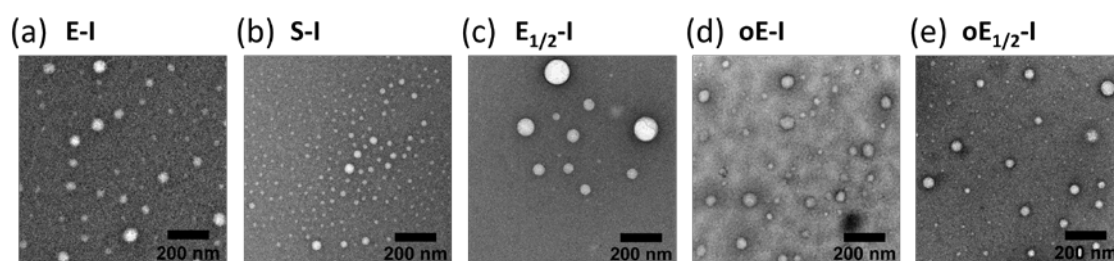


**Figure 3.** Negative stained TEM micrographs of the nanostructures formed by the different ELdcRs solutions (25  $\mu\text{M}$ ) at 37  $^{\circ}\text{C}$  in aqueous solution. All the ELdcR designs self-assembled into spherical micelles, even the highly asymmetric diblock designs (oE-I and oE<sub>1/2</sub>-I).

The evaluation of DLS data showed that non-ionic S-I diblock self-assembled into spherical nanoparticles ( $D_h = 35$  nm, PDI = 0.173 at  $25 \mu\text{M}$ ) with monomodal size distributions over the entire concentration range (Figure 4 and S4b). Additionally, increasing concentrations seemed to decrease  $D_h$  but did not affect neither micellar assembly nor polydispersity (FigureS5).

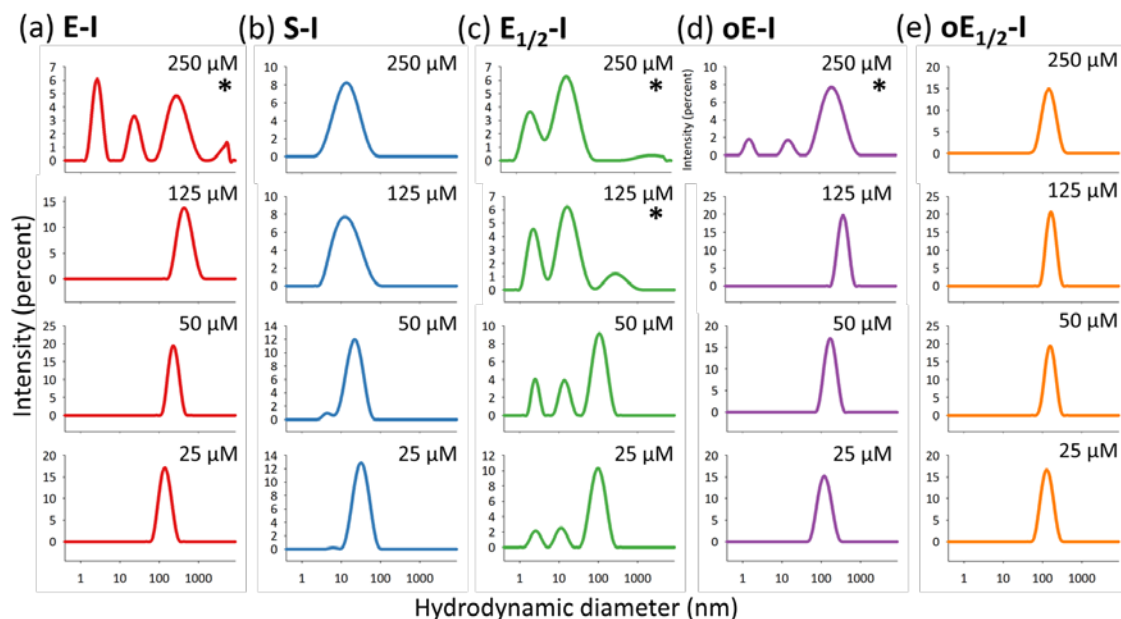


**Figure 4.** Intensity size distributions calculated by DLS of the nanostructures formed by the self-assembly of ELdcRs in aqueous solution in the concentration range 25-250  $\mu\text{M}$  at 37  $^{\circ}\text{C}$ . At high concentrations, in highly polydisperse samples, DLS size distributions may not be representative of the diameter of the nanostructures due to the limitations of the technique (\*).

In contrast, the presence of charged residues in the coronal block induced changes in the self-assembly which varied depending on hydrophilic block length and charge distribution.

Overall, a comparison of the DLS size distributions for the ionic ELdcRs revealed different tendencies for self-assembly as a function of the concentration. Firstly, although E-I diblock co-recombinamer exhibited similar hydrophilic weight fraction than S-I, it self-assembled into larger spherical nanoparticles ( $D_h = 142$  nm, PDI = 0.154 at  $25 \mu\text{M}$ ) whose  $D_h$  increased as a function of concentration. At  $250 \mu\text{M}$ , the micellar

structuration was compromised and the monomodal distribution evolved towards more complex distributions, as revealed by intensity plots and correlograms (Figure 4a and S4a, respectively). Secondly, halving the length of the anionic block in the  $E_{1/2}$ -I diblock co-recombinamer ( $f = 30\%$ ) impaired the polydispersity of the sample. The  $E_{1/2}$ -I micelles showed a multimodal distribution (PDI = 0.357 at  $25\ \mu\text{M}$ ) over the whole concentration range (Figure 4c and S4c and S5). Thirdly, spherical nanoparticles were also formed upon self-assembly of the highly asymmetric ELdcRs. The unbalanced ratio between the hydrophilic:hydrophobic block lengths (1:6 and 1:12 for oE-I and o $E_{1/2}$ -I, respectively), did not hinder micellar assembly. An increase in charge density in the corona stabilized the formation of spherical nanoparticles in solution and both asymmetric ELdcRs self-assembled into micelles with  $D_h$  similar to E-I at  $25\ \mu\text{M}$  ( $D_h = 137\ \text{nm}$  and PDI = 0.223 for oE-I, and  $D_h = 135\ \text{nm}$  and PDI = 0.115 for o $E_{1/2}$ -I). However, there were significant differences between both asymmetric ELdcRs. In the oE-I,  $D_h$  increased as a function of concentration thus showing a similar behavior than E-I. In contrast, as shown by the intensity size distributions and correlation functions, the  $D_h$  value for the o $E_{1/2}$ -I micelles remained constant over the whole concentration range (Figure 4e and S4e).

It is important to note that at high concentrations, DLS size distributions must be considered with caution due to the limitations of the technique. Concentrated samples may lead to multiple scattering and the intercept of the correlation curve due to a decrease on the scattering intensity (Figure S4). In addition, it may result in an increase in the polydispersity and a decrease on the mean diameter of the particles.<sup>43</sup> As such, size distributions labeled with a star (\*) in Figure 4 showed a low reproducibility and may not reflect the actual size and size-distribution of the nanostructures.

In order to resolve the above differences and gain deeper insight into the architecture of the formed structures, cryoTEM micrographs of ELdcR samples at high concentrations were obtained (Figure 5). Consistent with DLS results, non-charged SI diblock copolymer led to the assembly into spherical micelles across a wide polymer concentration range (25-500  $\mu\text{M}$ ). In contrast, ionic diblock designs triggered the formation of micellar aggregates at high concentrations. At 250  $\mu\text{M}$ , cryoTEM images of the E-I, E<sub>1/2</sub>-I and oE-I polymers suggested that intermolecular Coulomb repulsions between charged residues in the corona might destabilize the spherical assembly, thereby promoting the formation of micellar strings of different sizes and shapes. The tendency to form these supramicellar structures seemed to be influenced by the length of the coronal block, where five consecutive charged pentapeptides (oE<sub>1/2</sub>-I,  $f = 10\%$ ) were not sufficient to drive the assembly into micellar strings, thus resulting in spherical micelles over the whole concentration range, comparable to the non-ionic S-I diblock. Moreover, the presence of microaggregates in the E-I ( $f = 46\%$ ) sample at 250  $\mu\text{M}$  suggested that the longer ionic hydrophilic block, the greater the tendency to form supramicellar structures. It must also be noted that in E<sub>1/2</sub>-I and oE-I samples at 250  $\mu\text{M}$ , micellar and supramicellar conformations coexisted. At 500  $\mu\text{M}$ , the effect of the concentration drove the formation of larger interconnected micellar strings in E-I, E<sub>1/2</sub>-I and oE-I polymers, thus constituting the three-dimensional network of mesoscopic physical hydrogels.

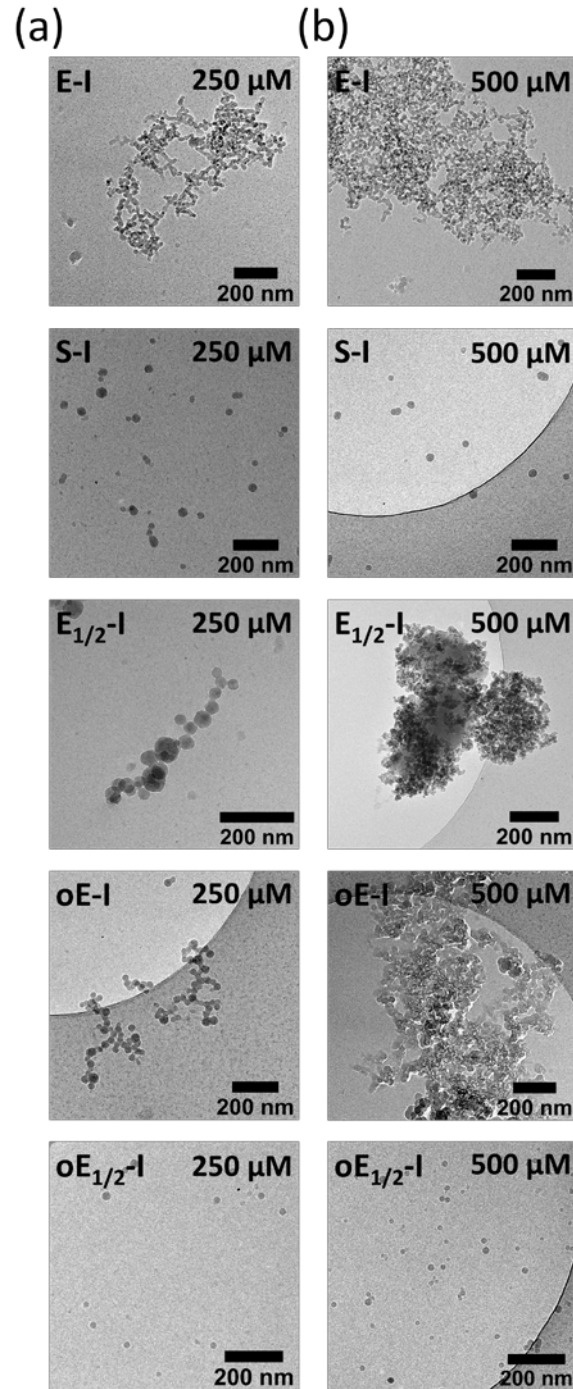


**Figure 5.** CryoTEM micrographs of the different diblock protein polymers. When concentration increases (above  $250 \mu\text{M}$ ), it drives the formation of hierarchical micelles aggregates in some of the ionic ELdcR designs (E-I,  $E_{1/2}$ -I and oE-I), whereas micellar assembly was favored in the others (S-I and  $oE_{1/2}$ -I).

Given that viscoelastic properties of a microstructured fluid can be determined by monitoring the thermal diffusive motion of tracer particles,<sup>44,45</sup> the effect of the polymer concentration on the self-assembly of ELdcRs was then monitored by DLS-based passive

microrheology. It is well established that the viscosity of protein solutions is strongly affected by the protein-protein interactions and the subsequent formation of supramolecular structures.<sup>46</sup> Thus, the evaluation of the viscosity-concentration relationship allowed for a quantitative comparison of the self-assembly characteristics of the different ELdcRs (Figure 6). As expected, the dependence of viscosity on polymer concentration was observed in all ELdcRs. Nevertheless, significant differences on relative viscosity values highlighted the formation of different supramolecular assemblies as observed by cryoTEM. The viscosity of ELdcRs that self-assembled into spherical micelles across all different concentrations (S-I and oE<sub>1/2</sub>-I) showed a slight increase with increasing concentration, a result similar to that typically observed of semidilute solutions of globular proteins.<sup>47</sup> The assembly into micellar strings and physical gels correlated with a more rapid increase in the viscosity of solutions of E-I, E<sub>1/2</sub>-I and oE-I. Additionally, the greater tendency to form supramicellar structures of the E-I diblock co-recombinamer could be noted, thus reaching higher viscosity values than the E<sub>1/2</sub>-I and the oE-I recombinamers.

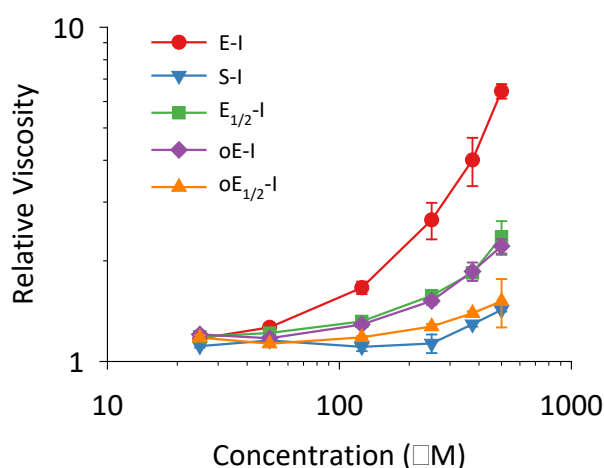


**Figure 6.** Comparison of the viscosity obtained by DLS-based microrheology of the ELdcRs at different concentrations. The formation of supramicellar assemblies led to an increase of the viscosity of the solution.

In addition to relative viscosity measurements, the effect on shear moduli of the ELdcR designs was also studied. Mean-square displacement (MSD,  $\langle \Delta r^2(t) \rangle$ ) of the tracer particles (Figure S6) can be utilized to infer a complex, frequency-dependent modulus,  $G^*$  via a generalized Stokes-Einstein equation.<sup>48</sup> At low concentrations, all the ELdcRs self-assembled into spherical nanoparticles and, as a consequence, no differences were found in the evolution of  $G^*(\omega)$  across the different samples (Figure S7a). However, the formation of supramicellar structures in E-I, E<sub>1/2</sub>-I and oE-I samples led to a decrease in the MSD slope (Figure S6a, S6c and S6d), thus reflecting an increase in the magnitude of  $G^*(\omega)$  (Figure S7b and S7c). In addition, substantial differences between these three diblock designs were observed with a greater tendency to form micellar aggregates, which was associated with a greater magnitude of  $G^*(\omega)$ .

Self-assembly of ionic synthetic co-polymer micelles into higher-level architectures is usually driven by electrostatic interactions.<sup>49</sup> To that end, electrostatic repulsion between charged coronas must be overcome and variations in the pH or addition of counterions. Interestingly, in the diblock co-recombinamers of the present study, the presence of charged residues seemed to be the driving force that triggered the self-assembly into higher-order architectures. We propose that the electrostatic repulsion between anionic glutamic acids induced defects in the corona of the micelle, thus partially exposing the hydrophobic cores which trigger the assembly of the ELdcR chains into supramicellar structures (Figure 7). Therefore, ionic block length and charge density strongly influence the tendency to undergo the hierarchical assembly and predetermine the viscoelastic properties of the higher-order structures. Consistent with previous studies with polyelectrolytes diblocks based on polypeptide sequences, any distortion to stabilize the packing of charged ionic blocks comes at a cost of

destabilization of the hydrophobic cores and hence, the hierarchical assembly into micellar strings and nanogels become present.<sup>50</sup>

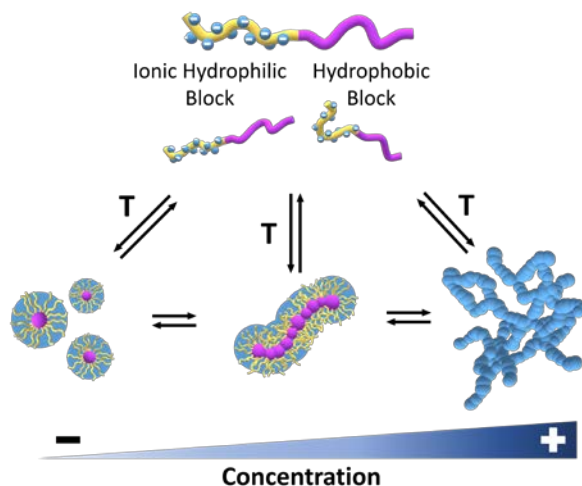


**Figure 7.** Model for ionic ELdcR hierarchical assembly. The LCST phase transition of the hydrophobic blocks (in violet) triggers the assembly into different supramolecular architectures (spherical micelles, micellar strings or physical hydrogels) as a function of the concentration.

### 3.4. Self-assembly into physically cross-linked hydrogels

Given that the E-I diblock co-recombinamer undergoes a phase transition towards physical hydrogels driven by concentration,<sup>25</sup> it was logical to investigate the influence of the corona composition on gelation. After incubation of 2.5 mM solutions of the ELdcRs at 37 °C, we found that only three ELdcRs, namely E-I, E<sub>1/2</sub>-I and oE-I, had undergone a phase transition (Figure 8). These findings are in line with nanostructure characterization on the nano- and mesoscale, and the tendency of to form supramicellar structures seems to be directly related to the ability to undergo gelation.

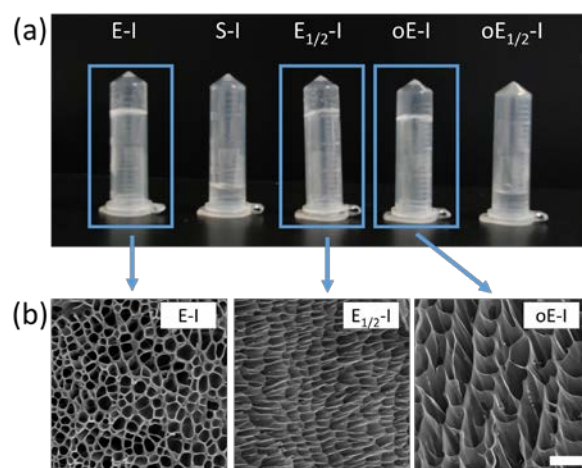


**Figure 8.** (a) Physical hydrogel formation in 2.5 mm solutions at 37 °C. (b) SEM micrographs of the cryo-fractured hydrogels. The size of all SEM images is 25 x 25  $\mu\text{m}$  and the size of scale bar is 4  $\mu\text{m}$ .

We characterized the rheological properties of the hydrogels in order to evaluate if the molecular design affects the viscoelastic properties.

First, the viscosity of the three hydrogels was measured as a function of shear rate using flow measurements. All three hydrogels exhibited a shear thinning behavior, with the hydrogel viscosity decreasing linearly by up to four orders of magnitude for the three orders of magnitude swept for shear rate (Figure 9).

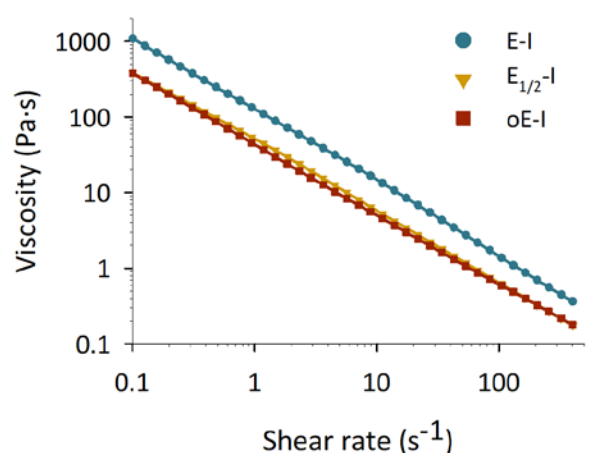


**Figure 9.** ELdcR hydrogel viscosity as a function of shear rate at 37 °C under continuous flow.

The linear viscoelastic region (LVR) was then determined by using dynamic measurements, specifically carrying out a sweep of the strain amplitude. As can be seen from Figure S8, no significant changes were observed in the complex modulus magnitude up to a strain amplitude of around 1%. A 0.3% strain was selected for all the oscillatory measurements in a trade-off between operating into the LVR and noise. Although SEM imaging of the hydrogel networks showed that the three hydrogels presented similarities in their microstructure (Fig. 8b), diverse rheological behaviors were observed. Figure 10 shows the frequency response of both the storage ( $G'$ ) and loss ( $G''$ ) moduli. While no noticeable dependence of  $G'$  on frequency was detected for E-I, this modulus exhibited frequency dependence for both  $E_{1/2}$ -I and oE-I hydrogels. Although at 1 Hz the higher storage modulus corresponds to E-I, the magnitude order of this modulus for the three hydrogels remains in the same range (Table 2).

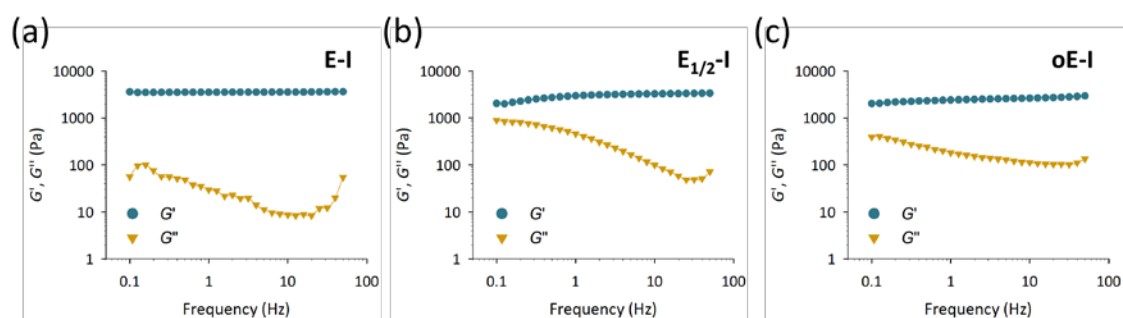


**Figure 10.** Rheological characterization of the physical hydrogels formed at 37 °C ELdcRs at the same molar concentration (2.5 mM in ultrapure water). Viscoelastic properties of the physically-crosslinked hydrogels varied substantially as a function of the hydrophilic block composition.

As for shear loss modulus ( $G''$ ), a clear frequency-dependence was observed in the three hydrogels at frequencies lower than 10 Hz. Nevertheless, the magnitude and the rate of decrease in the shear loss modulus varied significantly depending on the diblock composition. The shear loss modulus absolute value for  $E_{1/2}$ -I (480 Pa at 1 Hz) was considerably higher than that of oE-I and E-I (in a ratio of 2.7 and 15, respectively). At the highest frequencies, similar values of about 50 and 100 Pa were found for  $E_{1/2}$ -I and

oE-I, respectively. In the case of E-I and E<sub>1/2</sub>-I, the loss modulus decrease around a magnitude order when frequency change from 0.1 Hz to 10 Hz. Maxwell viscoelastic model foresees the decrease of  $G''$  with frequency when long relaxation times are assumed.<sup>51</sup>

**Table 2.** Mean  $G'$ ,  $G''$  and  $\delta$  for the different ELdcRs at 37 °C (2.5 mm in ultrapure water). Values were chosen from the LVE region (0.3% strain) at a frequency of 1 Hz.

	<b>E-I</b>	<b>E<sub>1/2</sub>-I</b>	<b>oE-I</b>
<b><math>G'</math> (Pa)</b>	3404.7±428.2	2824.3±261.3	2420.7±45.6
<b><math>G''</math> (Pa)</b>	32.03±2.2	480.2±58.6	180.9±5.2
<b><math>\delta</math> (degrees)</b>	0.55±0.05	9.7±1.57	4.27±0.05

The relative evolution of the storage and loss moduli with frequency is followed by the phase angle,  $\delta$ . A very high elastic behavior was suggested for E-I ( $f = 46\%$ ) hydrogels, since phase angles lower than 1° were obtained (Figure S9). Nevertheless, decreasing the length of the hydrophilic block strongly affected the elasticity of the gel, and then, a viscoelastic behavior emerged. The elastic behavior was partially lost in the other two hydrogels at low frequencies, especially for E<sub>1/2</sub>-I, where values of  $\delta$  higher than 10° were reached. The phase angle decreases around an order of magnitude when frequency change from 0.1 Hz to 10 Hz (Figure S9), indicating a strong decrease of the loss modulus with respect to the storage modulus in these hydrogels.

Above  $T_t$ , I-blocks underwent a hydrophobic collapse giving rise to transient secondary structures (e.g. type II  $\beta$ -turns), but maintaining conformational disorder and hydration. It has been demonstrated in literature that hydrophobic effect and chain entropy lead the elastic recoil of self-assembled elastomeric protein chains.<sup>52</sup> When the network of the hydrogel is deformed, the extension of the disordered hydrophobic blocks decreases the

chain entropy. Subsequently, the entropy of the chain is restored driving the elastic response upon stress release.

Since our system is stabilized by hydrophobic interactions, hydrophilic block composition is likely to play a crucial role in maintaining the structure of the hydrogel by keeping the hydrophobic cores in solution and hindering the chains from sliding past each other. Thus, hydrophilic block length seemed to contribute in preventing the perturbation of the micellar fiber network (Figure 11). The effect of halving the hydrophilic E-block in  $E_{1/2}$ -I ( $f = 30\%$ ) on the loss modulus supports this hypothesis. The evolution of the loss modulus with frequency (Figure 10b) indicated that, when stress was applied at low frequencies, the energy was dissipated generating greater viscous response in  $E_{1/2}$ -I and oE-I hydrogels than in E-I ones. We attribute the increase in dissipation energy to an increase in the molecular motion in the chains.

When the gel is deformed, the perturbed gel network would generate a partially exposed area of the hydrophobic cores, resulting in increased molecular motion and in molecular friction. Moreover, exchange or dissociation of the physical crosslinking domains may also occur.<sup>53</sup> These processes would also imply both the water molecules diffusion and spatial reorganization of the chains within the fibers of the hydrogel,<sup>54</sup> which requires long relaxation times. At low frequencies, which corresponds to a high timescale, the characteristic relaxation time of the above processes is roughly comparable to the timescales on which the hydrogel is deformed, and then, loss modulus changes are observed with frequency. On the contrary, at high frequencies, where the timescale of the stimulus signal is reduced, changes on the shear loss modulus could not be followed.

Hydrogels formed by oE-I diblocks also showed viscoelastic behavior, but with substantial differences. The highly asymmetric design ( $f = 17\%$ ) seemed to minimize

the effect of a reduced hydrophilic block length. This could be due to an increase in charge density. Electrostatic repulsion between charged residues may decrease the molecular motion and thus, the viscous behavior in favor of a more elastic network. In this case, the hydrogel viscoelastic properties may be modulated by the balance between the hydrophobic/hydrophilic block length and charge density.

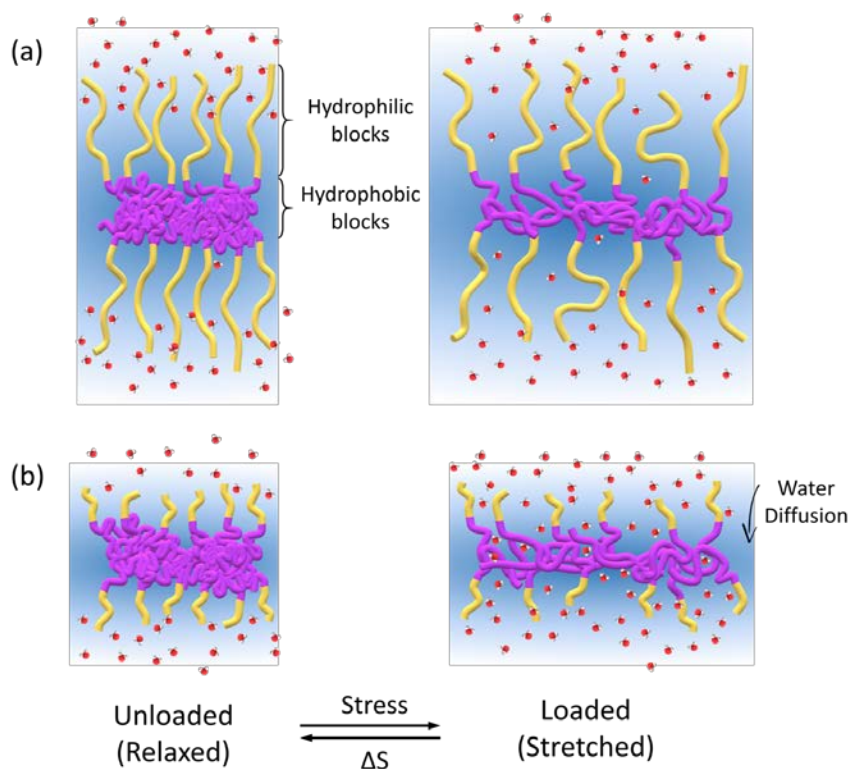


**Figure 11.** Schematic representation of the oscillatory shear response of the physical hydrogels based on ionic ELdcRs. Our findings provide support for a model of physical hydrogels in which the network is formed by the coacervation of the hydrophobic blocks of the ELdcRs. The hydrophilic block length and composition play a crucial role in the viscoelastic properties of the network. When applying shear stress, a balanced hydrophilic:hydrophobic block length ratio prevents the distortion of the network and lead to an elastic response (a). In contrast, a decrease in the hydrophilic block length leads to a partial exposition of hydrophobic cores, which results in a greater molecular reorganization and motion, thus increasing the dissipation energy (b).

Finally, rheological behavior of the three ELdcR-based hydrogels was measured at the same mass concentration. Given the difference in the length of the hydrophilic block and in the molecular weight of the resulting host protein polymer chains, we aimed to assess whether the different viscoelastic responses observed were due to the differences in the hydrophilic block composition or to the different mass concentration. Therefore,

oscillatory shear tests (strain and frequency sweeps, Figure S10 and Figure 12, respectively) were performed in the three hydrogels at a concentration of 11.7 % (w/v), which corresponds to 2.5 mM, 3.2 mM and 3.8 mM of the E-I, E<sub>1/2</sub>-I and oE-I, respectively.

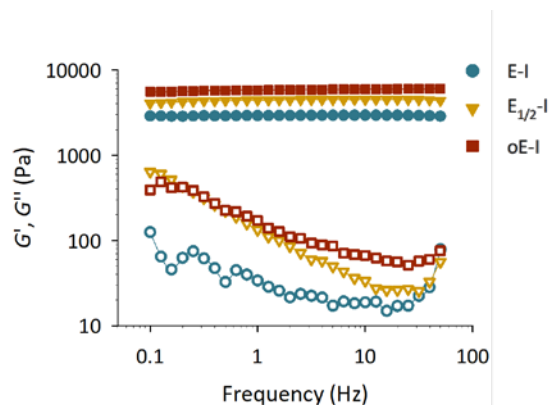


**Figure 12.** Oscillatory shear rheology frequency sweeps for E-I, E<sub>1/2</sub>-I and oE-I hydrogel at the same mass concentration (11.7 %). Closed and open symbols represent frequency dependence of the storage and loss shear moduli ( $G'$  and  $G''$ ), respectively.

As expected, different viscoelastic response to the frequency was observed for both storage and loss moduli in the three hydrogels in line with the rheological characterization at the same molar concentration (Figure 10). Shear moduli showed a frequency-dependence following the classical Maxwell model although with substantial differences in the magnitude.

As far as shear storage moduli ( $G'$ ) is concerned, the comparison between the three hydrogels at the same mass concentration revealed that increasing the molar concentration correlates with an increase in the stiffness of the hydrogel (Figure S10 and Figure 12). At a frequency of 1 Hz, storage modulus value was 2.9 kPa for E-I (2.5 mM), 4.4 kPa for E<sub>1/2</sub>-I (3.2 mM) and 5.8 kPa for oE-I (3.8 mM). This evidence supports our tentative model for hierarchical assembly in ELdcRs. Since phase transition of ELdcRs is mainly triggered by the thermally-driven coacervation of the hydrophobic I-blocks, the higher the number of molecules (higher molar concentration), the stiffer hydrogel. As such, an increase on the molar concentration would imply an increment of

the micellar strings, which would result in a denser hydrogel network and hence, on a higher stiffness.

Additionally, once again, the effect of hydrophilic block composition on the viscoelastic response was evinced. Despite that all the three hydrogels were prepared at the same mass concentration, their viscoelastic behavior was strongly varied due to ELdcR design differences. Halving the hydrophilic block in the E<sub>1/2</sub>-I radically affected the shear loss modulus. It led to an increase of roughly one order of magnitude at low frequencies comparing to E-I and a strong frequency dependence, characterized by a decay of around two orders. This frequency-dependence was minimized in the oE-I hydrogels probably due to the increased charge density. Thus, these results lend support to our model. Even though the gelation is driven by the LCST transition of the hydrophobic blocks, the composition of the hydrophilic block is crucial for the hierarchical assembly of the ELdcR-micelles and the properties of the resulting hydrogels in the meso-/micro- and macroscale. In light of these results, it is clear that ionic hydrophilic blocks play a critical role in the establishment of the network of the hydrogel and its strengthen. Indeed, the presence of charged residues in IDPPs with diblock designs contributes both hierarchical assembly and maintenance of network integrity.

#### **4. Conclusions**

The phase behavior of semidilute and concentrated solutions of IDPPs has been studied in order to evaluate the effect of charge distribution on the supramolecular assembly.

We have demonstrated that the length and charge distribution of ionic hydrophilic blocks play a crucial role in the hierarchical assembly of IDPPs with amphiphilic diblock designs. Firstly, increasing charge density in hydrophilic block of ELdcRs

overcomes the pre-established limits for the *de novo* design of spherical micelles based on IDPPs. Moreover, electrostatic repulsion between charged residues in the corona contributes to the assembly of highly asymmetric diblock co-recombinamers into micelles at low concentrations. Secondly, the presence of ionic residues drives an innovative mechanism of hierarchical self-assembly of micellar nanostructures into higher-order assemblies, such as micellar strings and physical hydrogels. Lastly, the effect of the length and charge distribution of the ionic block also contributes to the initiation of the liquid-gel transition and as a result, the mechanical properties of the subsequent hydrogels can be tuned by varying the composition of the ionic block. As such, this study represents a successful and novel step towards the design of hierarchically self-assembling nanosystems from IDPs and provides insight on the contribution of charge distribution on protein phase separation.

### **Supporting Information**

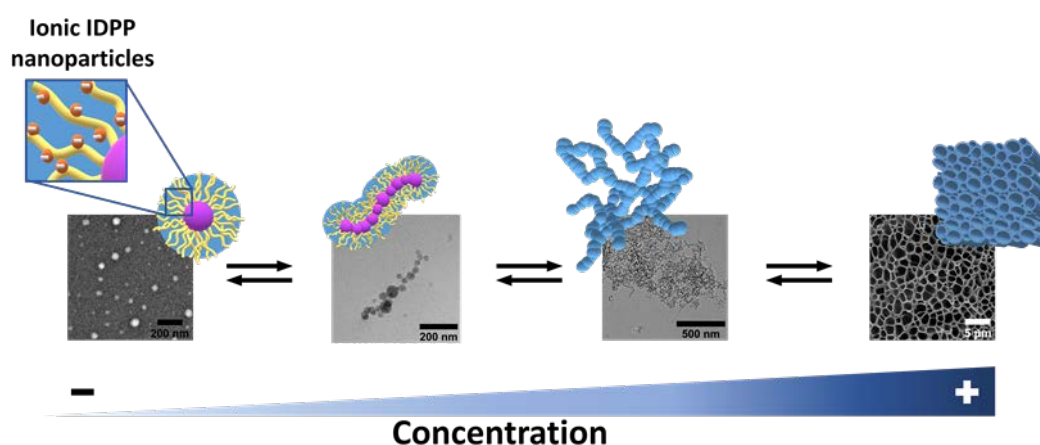
MALDI-TOF spectra (Figure S1 and S2) and comparison with the theoretical molecular weights (Table S1), HPLC analysis (Table S2), CD characterization (Figure S3), additional DLS data (Figure S4 and S5), microrheological characterization (MSD of the tracer particles, Figure S6 and frequency-dependence of the complex modulus, Figure S7), rheological characterization of the physical hydrogels: strain sweeps (Figure S8 and S10) and phase angle (Figure S9), (PDF)

### **ACKNOWLEDGEMENTS**

The authors acknowledge Ms. Rocío García for technical assistance during recombinant production. They also acknowledge the Servicio General de Apoyo a la Investigación-SAI (Universidad de Zaragoza) for technical support with the TEM and SEM data collection. The authors acknowledge Dr. Lubinda Mbundi for language editing of the

manuscript. The authors are grateful for funding from the European Commission (MSCA-ITN-2014-ETN-642687), the Spanish Government (MAT2016-78903-R, MAT2015-68901-R and PCIN-2015-010 (FunBioPlas)), Junta de Castilla y León (VA317P18) and Centro en Red de Medicina Regenerativa y Terapia Celular de Castilla y León.

## TABLE OF CONTENTS GRAPHIC



## REFERENCES

- (1) Jang, Y.; Champion, J. A. Self-Assembled Materials Made from Functional Recombinant Proteins. *Acc. Chem. Res.* **2016**, *49* (10), 2188–2198. <https://doi.org/10.1021/acs.accounts.6b00337>.
- (2) Yang, Y. J.; Holmberg, A. L.; Olsen, B. D. Artificially Engineered Protein Polymers. *Annu. Rev. Chem. Biomol. Eng.* **2017**, *8* (1), 549–575. <https://doi.org/10.1146/annurev-chembioeng-060816-101620>.
- (3) Roberts, S.; Dzuricky, M.; Chilkoti, A. Elastin-like Polypeptides as Models of Intrinsically Disordered Proteins. *FEBS Lett.* **2015**, *589* (19PartA), 2477–2486. <https://doi.org/10.1016/j.febslet.2015.08.029>.

- (4) Ruff, K. M.; Roberts, S.; Chilkoti, A.; Pappu, R. V. Advances in Understanding Stimulus-Responsive Phase Behavior of Intrinsically Disordered Protein Polymers. *J. Mol. Biol.* **2018**, *430* (23), 4619–4635. <https://doi.org/10.1016/J.JMB.2018.06.031>.
- (5) Pastuszka, M. K.; Janib, S. M.; Weitzhandler, I.; Okamoto, C. T.; Hamm-Alvarez, S.; MacKay, J. A. A Tunable and Reversible Platform for the Intracellular Formation of Genetically Engineered Protein Microdomains. *Biomacromolecules* **2012**, *13* (11), 3439–3444. <https://doi.org/10.1021/bm301090x>.
- (6) Simon, J. R.; Carroll, N. J.; Rubinstein, M.; Chilkoti, A.; López, G. P. Programming Molecular Self-Assembly of Intrinsically Disordered Proteins Containing Sequences of Low Complexity. *Nat. Chem.* **2017**, *9* (6), 509–515. <https://doi.org/10.1038/nchem.2715>.
- (7) Simon, J. R.; Egtesadi, S. A.; Dzuricky, M.; You, L.; Chilkoti, A. Engineered Ribonucleoprotein Granules Inhibit Translation in Protocells. *Mol. Cell* **2019**, *75* (1), 66–75.e5. <https://doi.org/10.1016/j.molcel.2019.05.010>.
- (8) Zhao, H.; Ibrahimova, V.; Garanger, E.; Lecommandoux, S. Dynamic Spatial Formation and Distribution of Intrinsically Disordered Protein Droplets in Macromolecularly Crowded Protocells. *Angew. Chemie - Int. Ed.* **2020**. <https://doi.org/10.1002/anie.202001868>.
- (9) Urry, D. W.; Trapane, T. L.; Prasad, K. U. Phase-Structure Transitions of the Elastin Polypentapeptide-Water System within the Framework of Composition-Temperature Studies. *Biopolymers* **1985**, *24* (12), 2345–2356. <https://doi.org/10.1002/bip.360241212>.
- (10) Despanie, J.; Dhandhukia, J. P.; Hamm-Alvarez, S. F.; MacKay, J. A. Elastin-like Polypeptides: Therapeutic Applications for an Emerging Class of Nanomedicines. *J. Control. Release* **2016**, *240*, 93–108. <https://doi.org/10.1016/j.jconrel.2015.11.010>.
- (11) Mcdaniel, J. R.; Mackay, J. A.; Quiroz, F. G.; Chilkoti, A. NIH Public Access. **2011**, *11*

- (4), 944–952. <https://doi.org/10.1021/bm901387t>.Recursive.
- (12) Saha, S.; Banskota, S.; Roberts, S.; Kirmani, N.; Chilkoti, A. Engineering the Architecture of Elastin-Like Polypeptides: From Unimers to Hierarchical Self-Assembly. *Adv. Ther.* **2020**, *3* (3), 1900164. <https://doi.org/10.1002/adtp.201900164>.
- (13) Acosta, S.; Quintanilla-Sierra, L.; Mbundi, L.; Rebotto, V.; Rodríguez-Cabello, J. C. Elastin-Like Recombinamers: Deconstructing and Recapitulating the Functionality of Extracellular Matrix Proteins Using Recombinant Protein Polymers. *Adv. Funct. Mater.* **2020**, 1909050. <https://doi.org/10.1002/adfm.201909050>.
- (14) Uversky, V. N. A Decade and a Half of Protein Intrinsic Disorder: Biology Still Waits for Physics. *Protein Sci.* **2013**, *22* (6), 693–724. <https://doi.org/10.1002/pro.2261>.
- (15) Das, R. K.; Pappu, R. V. Conformations of Intrinsically Disordered Proteins Are Influenced by Linear Sequence Distributions of Oppositely Charged Residues. *Proc. Natl. Acad. Sci.* **2013**, *110* (33), 13392–13397. <https://doi.org/10.1073/PNAS.1304749110>.
- (16) Pak, C. W.; Kosno, M.; Holehouse, A. S.; Padrick, S. B.; Mittal, A.; Ali, R.; Yunus, A. A.; Liu, D. R.; Pappu, R. V.; Rosen, M. K. Sequence Determinants of Intracellular Phase Separation by Complex Coacervation of a Disordered Protein. *Mol. Cell* **2016**, *63* (1), 72–85. <https://doi.org/10.1016/J.MOLCEL.2016.05.042>.
- (17) MacKay, J. A.; Callahan, D. J.; FitzGerald, K. N.; Chilkoti, A. Quantitative Model of the Phase Behavior of Recombinant PH-Responsive Elastin-like Polypeptides. *Biomacromolecules* **2010**, *11* (11), 2873–2879. <https://doi.org/10.1021/bm100571j>.
- (18) Mills, C. E.; Michaud, Z.; Olsen, B. D. Elastin-like Polypeptide (ELP) Charge Influences Self-Assembly of ELP–MCherry Fusion Proteins. *Biomacromolecules* **2018**, *19* (7), 2517–2525. <https://doi.org/10.1021/acs.biomac.8b00147>.

- (19) Bravo-Anaya, L. M.; Garbay, B.; Nando-Rodríguez, J. L. E.; Carvajal Ramos, F.; Ibarboure, E.; Bathany, K.; Xia, Y.; Rosselgong, J.; Joucla, G.; Garanger, E.; Lecommandoux, S. Nucleic Acids Complexation with Cationic Elastin-like Polypeptides: Stoichiometry and Stability of Nano-Assemblies. *J. Colloid Interface Sci.* **2019**, *557*, 777–792. <https://doi.org/10.1016/j.jcis.2019.09.054>.
- (20) Dreher, M. R.; Simnick, A. J.; Fischer, K.; Smith, R. J.; Patel, A.; Schmidt, M.; Chilkoti, A. Temperature Triggered Self-Assembly of Polypeptides into Multivalent Spherical Micelles. *J. Am. Chem. Soc.* **2008**, *130* (2), 687–694. <https://doi.org/10.1021/ja0764862>.
- (21) Hassouneh, W.; Zhulina, E. B.; Chilkoti, A.; Rubinstein, M. Elastin-like Polypeptide Diblock Copolymers Self-Assemble into Weak Micelles. *Macromolecules* **2015**, *48* (12), 4183–4195. <https://doi.org/10.1021/acs.macromol.5b00431>.
- (22) McDaniel, J. R.; Macewan, S. R.; Li, X.; Radford, D. C.; Landon, C. D.; Dewhirst, M.; Chilkoti, A. Rational Design of “Heat Seeking” Drug Loaded Polypeptide Nanoparticles That Thermally Target Solid Tumors. *Nano Lett.* **2014**, *14* (5), 2890–2895. <https://doi.org/10.1021/nl5009376>.
- (23) Widder, K.; MacEwan, S. R.; Garanger, E.; Núñez, V.; Lecommandoux, S.; Chilkoti, A.; Hinderberger, D. Characterisation of Hydration and Nanophase Separation during the Temperature Response in Hydrophobic/Hydrophilic Elastin-like Polypeptide (ELP) Diblock Copolymers. *Soft Matter* **2017**, *13* (9), 1816–1822. <https://doi.org/10.1039/C6SM02427K>.
- (24) Lee, T. A. T.; Cooper, A.; Apkarian, R. P.; Conticello, V. P. Thermo-Reversible Self-Assembly of Nanoparticles Derived from Elastin-Mimetic Polypeptides. *Adv. Mater.* **2000**, *12* (15), 1105–1110. [https://doi.org/10.1002/1521-4095\(200008\)12:15<1105::AID-ADMA1105>3.0.CO;2-1](https://doi.org/10.1002/1521-4095(200008)12:15<1105::AID-ADMA1105>3.0.CO;2-1).
- (25) Misbah, M. H.; Quintanilla, L.; Alonso, M.; Rodríguez-Cabello, J. C. Evolution of

- Amphiphilic Elastin-like Co-Recombinamer Morphologies from Micelles to a Lyotropic Hydrogel. *Polymer (Guildf)*. **2015**, *81* (81), 37–44.  
<https://doi.org/10.1016/j.polymer.2015.11.013>.
- (26) Huber, M. C.; Schreiber, A.; von Olshausen, P.; Varga, B. R.; Kretz, O.; Joch, B.; Barnert, S.; Schubert, R.; Eimer, S.; Kele, P.; Schiller, S. M. Designer Amphiphilic Proteins as Building Blocks for the Intracellular Formation of Organelle-like Compartments. *Nat. Mater.* **2015**, *14* (1), 125–132. <https://doi.org/10.1038/nmat4118>.
- (27) Schreiber, A.; Huber, M. C.; Schiller, S. M. A Prebiotic Protocell Model Based on Dynamic Protein Membranes Accommodating Anabolic Reactions. *bioRxiv* **2018**, 463356. <https://doi.org/10.1101/463356>.
- (28) Schreiber, A.; Stühn, L. G.; Huber, M. C.; Geissinger, S. E.; Rao, A.; Schiller, S. M. Self-Assembly Toolbox of Tailored Supramolecular Architectures Based on an Amphiphilic Protein Library. *Small* **2019**, 1900163.  
<https://doi.org/10.1002/sml.201900163>.
- (29) Rodríguez-Cabello, J. C.; Girotti, A.; Ribeiro, A.; Arias, F. J. Synthesis of Genetically Engineered Protein Polymers (Recombinamers) as an Example of Advanced Self-Assembled Smart Materials. In *Nanotechnology in Regenerative Medicine. Methods and Protocols*; Navarro, M., Planell, J. A., Eds.; Humana Press: Totowa, NJ, 2012; Vol. 811, pp 17–38. [https://doi.org/10.1007/978-1-61779-388-2\\_2](https://doi.org/10.1007/978-1-61779-388-2_2).
- (30) Gasteiger, E.; Hoogland, C.; Gattiker, A.; Duvaud, S.; Wilkins, M. R.; Appel, R. D.; Bairoch, A. Protein Identification and Analysis Tools on the ExPASy Server. In *The Proteomics Protocols Handbook*; Humana Press: Totowa, NJ, 2005; pp 571–607.  
<https://doi.org/10.1385/1-59259-890-0:571>.
- (31) Kyte, J.; Doolittle, R. F. A Simple Method for Displaying the Hydrophobic Character of a Protein. *J. Mol. Biol.* **1982**, *157* (1), 105–132. <https://doi.org/10.1016/0022->

2836(82)90515-0.

- (32) Micsonai, A.; Wien, F.; Kernya, L.; Lee, Y.-H.; Goto, Y.; Réfrégiers, M.; Kardos, J. Accurate Secondary Structure Prediction and Fold Recognition for Circular Dichroism Spectroscopy. *Proc. Natl. Acad. Sci. U. S. A.* **2015**, *112* (24), E3095-103. <https://doi.org/10.1073/pnas.1500851112>.
- (33) Micsonai, A.; Wien, F.; Bulyáki, É.; Kun, J.; Moussong, É.; Lee, Y.-H.; Goto, Y.; Réfrégiers, M.; Kardos, J. BeStSel: A Web Server for Accurate Protein Secondary Structure Prediction and Fold Recognition from the Circular Dichroism Spectra. *Nucleic Acids Res.* **2018**, *46* (W1), W315–W322. <https://doi.org/10.1093/nar/gky497>.
- (34) García-Arévalo, C.; Bermejo-Martín, J. F.; Rico, L.; Iglesias, V.; Martín, L.; Rodríguez-Cabello, J. C.; Arias, F. J. Immunomodulatory Nanoparticles from Elastin-like Recombinamers: Single-Molecules for Tuberculosis Vaccine Development. *Mol. Pharm.* **2013**, *10* (2), 586–597. <https://doi.org/10.1021/mp300325v>.
- (35) Janib, S. M.; Pastuszka, M.; Aluri, S.; Folchman-Wagner, Z.; Hsueh, P.-Y.; Shi, P.; Yi-An; Cui, H.; Mackay, J. A. A Quantitative Recipe for Engineering Protein Polymer Nanoparticles. *Polym. Chem.* **2014**, *5* (5), 1614–1625. <https://doi.org/10.1039/C3PY00537B>.
- (36) Quiroz, F. G.; Chilkoti, A. Sequence Heuristics to Encode Phase Behaviour in Intrinsically Disordered Protein Polymers. *Nat. Mater.* **2015**, *14* (11), 1164–1171. <https://doi.org/10.1038/nmat4418>.
- (37) Li, N. K.; Fuss, W. H.; Tang, L.; Gu, R.; Chilkoti, A.; Zauscher, S.; Yingling, Y. G. Prediction of Solvent-Induced Morphological Changes of Polyelectrolyte Diblock Copolymer Micelles. *Soft Matter* **2015**, *11* (42), 8236–8245. <https://doi.org/10.1039/c5sm01742d>.

- (38) Meyer, D. E.; Chilkoti, A. Quantification of the Effects of Chain Length and Concentration on the Thermal Behavior of Elastin-like Polypeptides. *Biomacromolecules* **2004**, *5* (3), 846–851. <https://doi.org/10.1021/bm034215n>.
- (39) Kurzbach, D.; Hassouneh, W.; McDaniel, J. R.; Jaumann, E. A.; Chilkoti, A.; Hinderberger, D. Hydration Layer Coupling and Cooperativity in Phase Behavior of Stimulus Responsive Peptide Polymers. *J. Am. Chem. Soc.* **2013**, *135* (30), 11299–11308. <https://doi.org/10.1021/ja4047872>.
- (40) Yamaoka, T.; Tamura, T.; Seto, Y.; Tada, T.; Kunugi, S.; Tirrell, D. A. Mechanism for the Phase Transition of a Genetically Engineered Elastin Model Peptide (VPGIG)<sub>40</sub> in Aqueous Solution. *Biomacromolecules* **2003**, *4* (6), 1680–1685. <https://doi.org/10.1021/bm034120l>.
- (41) Borisov, O. V.; Zhulina, E. B. Morphology of Micelles Formed by Diblock Copolymer with a Polyelectrolyte Block. *Macromolecules* **2003**, *36* (26), 10029–10036. <https://doi.org/10.1021/ma0304628>.
- (42) Borisov, O. V.; Zhulina, E. B.; Leermakers, F. A. M.; Müller, A. H. E. Self-Assembled Structures of Amphiphilic Ionic Block Copolymers: Theory, Self-Consistent Field Modeling and Experiment. In *Self Organized Nanostructures of Amphiphilic Block Copolymers I*; Müller, A. H. E., Borisov, O., Eds.; Springer, Berlin, Heidelberg, 2011; Vol. 241, pp 57–129. [https://doi.org/10.1007/12\\_2011\\_114](https://doi.org/10.1007/12_2011_114).
- (43) Pecora, R. *Dynamic Light Scattering: Applications of Photon Correlation Spectroscopy*; Pecora, R., Ed.; Plenum Press: New York and London, 1985. [https://doi.org/10.1007/978-1-4020-4465-6\\_13](https://doi.org/10.1007/978-1-4020-4465-6_13).
- (44) Zia, R. N. Active and Passive Microrheology: Theory and Simulation. *Annu. Rev. Fluid Mech.* **2018**, *50* (1), 371–405. <https://doi.org/10.1146/annurev-fluid-122316-044514>.

- (45) Furst, E. M.; Squires, T. M. *Microrheology*; Furst, E. M., Squires, T. M., Eds.; Oxford University Press: Oxford, UK, 2018.  
<https://doi.org/10.1093/oso/9780199655205.001.0001>.
- (46) Zhang, Z.; Liu, Y. Recent Progresses of Understanding the Viscosity of Concentrated Protein Solutions. *Curr. Opin. Chem. Eng.* **2017**, *16*, 48–55.  
<https://doi.org/10.1016/j.coche.2017.04.001>.
- (47) Amin, S.; Rega, C. A.; Jankevics, H. Detection of Viscoelasticity in Aggregating Dilute Protein Solutions through Dynamic Light Scattering-Based Optical Microrheology. *Rheol. Acta* **2012**, *51* (4), 329–342. <https://doi.org/10.1007/s00397-011-0606-6>.
- (48) Mason, T. G.; Weitz, D. A. Optical Measurements of Frequency-Dependent Linear Viscoelastic Moduli of Complex Fluids. *Phys. Rev. Lett.* **1995**, *74* (7), 1250–1253.  
<https://doi.org/10.1103/PhysRevLett.74.1250>.
- (49) Lu, Y.; Lin, J.; Wang, L.; Zhang, L.; Cai, C. Self-Assembly of Copolymer Micelles: Higher-Level Assembly for Constructing Hierarchical Structure. *Chem. Rev.* **2020**, *120* (9), 4111–4140. <https://doi.org/10.1021/acs.chemrev.9b00774>.
- (50) Nowak, A. P.; Breedveld, V.; Pine, D. J.; Deming, T. J. Unusual Salt Stability in Highly Charged Diblock Co-Polypeptide Hydrogels. *J. Am. Chem. Soc.* **2003**, *125* (50), 15666–15670. <https://doi.org/10.1021/ja0381050>.
- (51) Annable, T.; Buscall, R.; Ettelaie, R.; Whittlestone, D. The Rheology of Solutions of Associating Polymers: Comparison of Experimental Behavior with Transient Network Theory. *J. Rheol. (N. Y. N. Y.)* **1993**, *37* (4), 695–726. <https://doi.org/10.1122/1.550391>.
- (52) Rauscher, S.; Pomès, R. The Liquid Structure of Elastin. *Elife* **2017**, *6* (e26526), 1–21.  
<https://doi.org/10.7554/eLife.26526>.
- (53) Dooling, L. J.; Buck, M. E.; Zhang, W. Bin; Tirrell, D. A. Programming Molecular

Association and Viscoelastic Behavior in Protein Networks. *Adv. Mater.* **2016**, *28* (23), 4651–4657. <https://doi.org/10.1002/adma.201506216>.

- (54) Caccavo, D.; Cascone, S.; Lamberti, G.; Barba, A. A. Hydrogels: Experimental Characterization and Mathematical Modelling of Their Mechanical and Diffusive Behaviour. *Chem. Soc. Rev.* **2018**, *47* (7), 2357–2373. <https://doi.org/10.1039/c7cs00638a>.